ELSEVIER

Original Article

The impact of post manufacturing treatment of functionally graded Ti6Al4V scaffolds on their surface morphology and mechanical strength

D. Khrapov[a], A. Koptyug[b], K. Manabaev[a], F. Léonard[c], T. Mishurova[c], G. Bruno[c,d], D. Cheneler[e], K. Loza[f], M. Epple[f], R. Surmenev[a], M. Surmeneva[a,]*

[a] *National Research Tomsk Polytechnic University, 30 Lenina avenue, Tomsk 634050, Russia*
[b] *Mid Sweden University, Akademigatan 1, Östersund SE-831 25, Sweden*
[c] *Bundesanstalt für Materialforschung und -prüfung (BAM), Unter den Eichen 87, Berlin 12205, Germany*
[d] *University of Potsdam, Institute of Physics and Astronomy, Karl-Liebknecht-Str.24-24, 14476 Potsdam, Germany*
[e] *Lancaster University, Bailrigg, Lancaster LA1 4YW, United Kingdom*
[f] *Inorganic Chemistry and Center for Nanointegration Duisburg-Essen (CeNIDE), University of Duisburg-Essen, 45117 Essen, Germany*

ARTICLE INFO

ABSTRACT

An ultrasonic vibration post-treatment procedure was suggested for additively manufactured lattices. The aim of the present research was to investigate mechanical properties and the differences in mechanical behavior and fracture modes of Ti6Al4V scaffolds treated with traditional powder recovery system (PRS) and ultrasound vibration (USV). Scanning electron microscopy (SEM) was used to investigate the strut surface and the fracture surface morphology. X-ray computed tomography (CT) was employed to evaluate the inner structure, strut dimensions, pore size, as well as the surface morphology of additively manufactured porous scaffolds. Uniaxial compression tests were conducted to obtain elastic modulus, compressive ultimate strength and yield stress. Finite element analysis was performed for a body-centered cubic (BCC) element-based model and for CT-based reconstruction data, as well as for a two-zone scaffold model to evaluate stress distribution during elastic deformation. The scaffold with PRS post treatment displayed ductile behavior, while USV treated scaffold displayed fragile behavior. Double barrel formation of PRS treated scaffold was observed during deformation. Finite element analysis for the CT-based reconstruction revealed the strong impact of surface morphology on the stress distribution in comparison with BCC cell model because of partially molten metal particles on the surface of struts, which usually remain unstressed.

1. Introduction

Electron beam melting (EBM®) is a metal powder bed fusion additive manufacturing (AM) technology that makes the fabrication of complex porous constructions possible, in particular

* *Corresponding author.*
   E-mail: surmenevamaria@mail.ru (M. Surmeneva).

of porous components constructed of periodically repeating unit cells. Open cellular structures, such as diamond structure [1] or hatched structure [2] fabricated in Ti6Al4V using EBM process have been widely investigated for tissue scaffolds and low stiffness implants that approximate the mechanical properties of natural bone. After being implanted in the human body, the scaffold will not only bear the load caused by muscle action and gravity, but also facilitate and guide bone tissue regeneration, as Ma et al. demonstrated [3]. During the service life, all strain that the scaffold experiences should be resulting in only elastic deformation. Bone systems adaption to mechanical conditions includes increasing bone mass in dynamically loaded areas and decreasing bone mass in statically loaded or unloaded ones. Designing implants with needed mechanical properties and functionality basing entirely on mimicking natural structures is a promising approach. This approach is challenging both in terms of topology generation, and in manufacturing such complex structures. Today majority of the manufactured implants are still using only solid sections. But the mismatch between the stiffness of the solid implants, e.g. prosthetic stems and the patient's bone results in stress shielding extensively described by Harryson [4]. This can lead to bone resorption and eventual loosening of the implant. It is possible to avoid such effect reducing mismatch in stiffness between the implant and the bone. Porous metals represent a promising approach for reducing such stiffness mismatch and avoiding stress-shielding effects, different types and techniques of porous metals fabrication were by described by [5].

Yavari et al. proposed to use the term "metamaterials" when dealing with cell-based structures having microscale units [6]. Thus, a metamaterial can be considered a mechanical structure as far as its small-scale features and properties are concerned. At the same time, it behaves like a homogeneous material when macroscopic properties are analyzed. In this respect, a metamaterial is assumed to represent a continuous medium, and it makes sense to use commonly defined elastic moduli for characterizing its mechanical behavior. Manipulation of metamaterial properties, for example density, can be a key feature to mimic human bone properties. Accordingly, mechanical properties of additively manufactured functionally graded scaffolds with cubic cell structure with different porosity levels [7], BCC unit cell structure [8], rhombic dodecahedron unit cell structure [9] and Schwartz diamond unit cell structure [10] were investigated.

Although EBM technology offers the possibility for manufacturing highly porous components with high precision, the needed post-processing, for example etching [11], can have a serious impact on the properties of the components. Therefore, the impact of post-processing methods on the mechanical properties needs to be investigated. The average powder size used for EBM process is larger than for laser-based powder bed process [12]. Powder grain sizes between 75 and 125–150 micron are specified as recommended by EBM machine manufacturer. Therefore, for the same size of the interconnected pores of the EBM- manufactured specimen partially sintered powder particles are stronger bonded together, and powder recovery needs a more complicated procedure. The EBM struts exhibit much rougher surface compared with the SLM-made struts caused by the sintered

particles [12]. With EBM, all solid parts of the manufactured components are surrounded by residual semi-sintered powder, and metal surfaces have partially embedded powder particles. Residual sintered powder remaining between the struts of manufactured porous structures and scaffolds should be removed during post-processing. If such powder is not completely removed it may become loose during service life of the component, and it can strongly influence the mechanical behavior of the whole component, for example making it effectively more ductile helping to re-distribute the stress from the critical areas. However, as the distribution of remaining sintered powder inside the porous structure is irregular, and in many cases simple optical inspection after post processing would not reveal such problems, the behavior of the structures thus becomes unpredictable. Also, mechanical loading of the porous structures with remaining powder facilitates the powder release, which is inacceptable in the majority of applications including the biomedical ones [13].

Arcam EBM, the manufacturer of electron beam melting equipment strongly recommends using specialized powder recovery system (PRS). It uses an air jet with working powder for the semi-sintered powder removal in all cases, including lattice structures. However, an air jet loses powder removal efficiency when penetrating into narrow deep holes and inner layers of porous structures making dense lattice cleaning quite problematic. The quality of standard PRS powder removal was investigated earlier by Drescher et al. [14]. A linear dependency between pore size and depth of air jet penetration into the structure was found: the denser lattice causes more difficulties with powder particle removal. Frictional forces and airflow dynamics in the narrow channels with rough surface and the mutual anchoring of particles are the main factors responsible for this. One can also expect additional problems with increasing time of PRS treatment: it was found that sand blasting creates many tiny cracks and leads to additional roughness of the component surfaces [15].

Chemical etching mainly applied for surface post-processing of the component manufactured by EBM [16] and SLM [17] methods was also investigated as a method for sintered powder removal. However, etching also leads to the generation of small and shallow pits on the component surfaces with a diameter of 2–10 μm [15]. In addition, aggressive etching substances can remain in the pits and can be released during the component lifetime. While the process is effective, it tends to erode material indiscriminately, hence compromising dimensional accuracy of the components [18]. Re-melting strategies with different directions can decrease surface roughness and porosity [19], but this method can be implemented only for bulk specimens. Laser polishing as a technique reducing surface roughness that involves the melting of a thin layer of substrate, with surface tension causing the material to flow from peaks to valleys [20]. However, re-melting the surface could further disturb the residual stress or even result in undesirable changes in surface chemistry [21]. Laser polishing depending on the proper laser beam focusing is hardly appropriate for treating porous structures, where some of the struts inside the structure are completely shadowed by the surface layers. Moreover, laser polishing can cause deformation of struts because the size of partially molten particles becomes comparable to the thickness of struts. Ultra-

sonic treatment is also used for AM parts, for example in rotary ultrasonic machining (RUM) [22], ultrasonic cavitation abrasive finishing (UCAF) [23] or ultrasonic cleaners [24].

During consultations with EBM equipment manufacturer R&D Department on improving semi-sintered powder removal from EBM-manufactured structures, it was suggested to try ultrasonic vibration (USV) cleaning with direct contact of vibration actuator and a component. According to the preliminary trials with the solid structures having long inner channels, powder was effectively loosened from the solid material boundary. Together with subsequent cleaning using PRS system, it was more efficient than ultrasonic bath cleaning. An additional rationale for direct ultrasonic cleaning was to avoid contact of implant surfaces with surfactants or other chemicals often added into ultrasonic bath to facilitate better powder removal. To the best of our knowledge, there are no open publications on using ultrasonic cleaning with direct ultrasonic actuator contact outside liquid media.

The aim of the current research was to determine mechanical properties investigate the difference in mechanical behavior and fracture modes of PRS and USV treated Ti6Al4V functionally graded scaffolds.

2. Materials and methods

2.1. Scaffolds fabrication

Porous scaffolds of Ti6Al4V alloy were fabricated by EBM system (Arcam EBM, Mölndal, Sweden) using standard parameter settings provided by equipment manufacturer. The structures were built layer-by-layer using a precursor Ti6Al4V powder (Arcam AB, Mölndal, Sweden) with particle size distribution of $75-125\,\mu m$. The scaffold design providing low effective elastic modulus was chosen for the present investigation. The AM equipment used in the present study was described elsewhere [25]. The build was maintained at a constant temperature of $740\,°C$ and a layer thickness of $50\,\mu m$ was employed.

The current research continues the work on scaffold characterization that was initiated earlier by Surmeneva et al. [26], where mechanical properties of different multiple-layered gradient scaffolds were studied. The newly manufactured scaffolds have identical design: a cylinder with an overall height of 30 mm and a diameter of 15 mm (Fig. 1) with a central full-length borehole of 5 mm in diameter and two layers of lattice with different basic unit cells. The cylinder consisted of two coaxial zones with different lattice structure density. The outer zone had a denser structure to imitate cortical bone, whereas the inner zone with an outer diameter of 11 mm had a less dense structure to imitate trabecular bone. Outer and inner zones consist of body centered cubic (BCC) elemental cells that are widely used in AM of porous and graded lattice structures, for example by Maskery et al. [27]. Lattice unit cell basic dimensions of 1.25 mm and 1.5 mm were used for the outer and inner zones, respectively. The boundary of the outer zone crosses the nodes of 1.25 mm lattice, the boundary of the inner zone passes across the centers of struts of 1.5 mm lattice cells.

The effectiveness of the powder recovery system was demonstrated in the simple porous structures earlier [14]. The effect of the cleaning procedures on the functionally graded porous structures, especially the ones having denser sections, is poorly investigated, though the transition between zones with different porosity can be problematic as for whole structure cleaning. The main advantage of the graded lattices is in mimicking the load bearing bones, therefore the effect of the traditional PRS and novel USV treatment on these structures is of interest.

2.2. Post-processing

The standard powder recovery system (PRS) by Arcam EBM uses a particle-blasting technology, simultaneously cleaning the components from semi-sintered powder and collecting the powder for recycling (Fig. 2a). With the PRS post-processing two specimens were taken from the EBM build and processed for powder removal in the PRS system working with air pressure of 5 bar [14]. The PRS treatment procedure was carried out until the sintered powder was no longer visible when looking through the structure against bright background.

Powder removal utilizing the ultrasonic vibration (USV) was carried out in two steps. Five identical specimens from the same EBM build were initially cleaned with powder recovery system as specified by EBM equipment manufacturer. In the second step additional cleaning was performed using USV system based on the commercial Sonic SwissBoster 20 kHz 1:1.5 Alu equipment originally designed for polymer welding. USV actuator head of the commercial system is mounted to the modified stand of the commercial table drill with added reinforcement bottom plate and fixation for the ultrasonic vibration head (Fig. 2b). Power supply from the commercial USV system (not shown in the figure) allows for adjusting the vibration power. Cleaning was performed in a single step by gently compressing the flat surfaces of the cylindrical scaffold samples between the face of vibrator and bottom plate (equivalent force ~5 N), and switching the power for 5–6 seconds at 75 % of maximum power. It was clear that PRS procedure was not able to completely remove the semi-sintered powder from the deeper layers of the scaffold, as small amount of powder was appearing over the bottom plate after USV cleaning of each sample. Similar inspection of the samples against a bright background was performed and no visible remains of semi-sintered powder inside the structure were left visible after USV treatment.

2.3. Scanning electron microscopy

The strut surface morphology and the fracture surface morphology were studied by scanning electron microscopy SEM, FEI Quanta 400 ESEM FEG equipped with energy-dispersive X-ray spectroscopy (EDX; Genesis 4000, SUTW-Si (Li) detector) operating in a high vacuum mode.
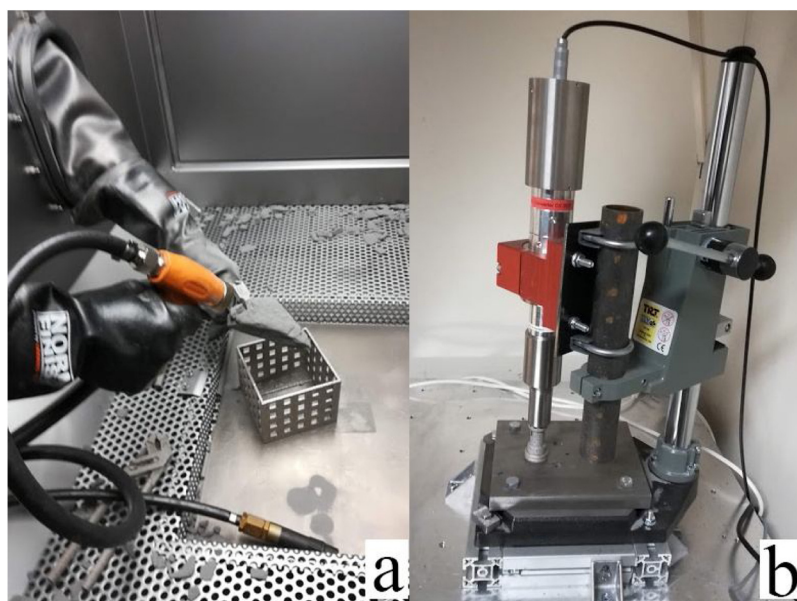
2.4. X-ray computed tomography

X-ray computed tomography (CT) was used to evaluate the inner structure, strut dimensions, pore size, and surface roughness and morphology of the porous scaffolds. The high resolution of the method allows studying shapes of individual scaffold elements, distribution of defects, surface roughness,
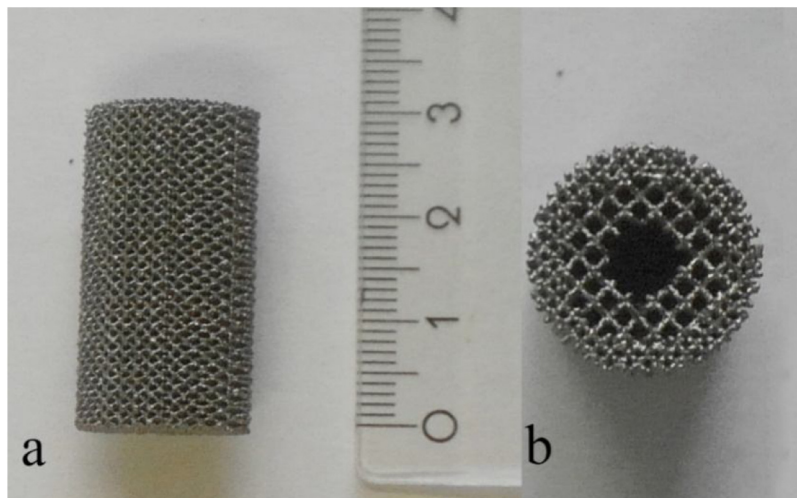
Fig. 1 – Two-zone scaffold: (a) side view, (b) top view.

Fig. 2 – Post-treatment methods: (a) powder recovery system (PRS), (b) ultrasonic vibration (USV) component treatment setup.

presence of unmolten or partially molten powder particles as well as the cracks [28]. Computed tomography was performed using a V|tome|x L 180/300 system from General Electrics working with X-ray tube voltage of 135 kV and a current of 70 μA and a voxel size of 18.5 μm. The data were processed using FiJi ImageJ software. VG Studio Max 3.1 and AvizoFire 8.4 software packages were used for image analysis and 3D rendering [29]. For each volumetric pore, a set of parameters including volume and sphericity were determined by the pore analysis tool from VG Studio Max 3.1.

Computed tomography was conducted for two of USV and two of PRS treated specimens before mechanical testing, and for one of USV and one of PRS treated specimens after mechanical testing.

The profile of the surface irregularities was extracted from the CT based images [28]. The average roughness (Ra) and the maximum height of the profile (Rt) were obtained according

to the ISO 4288:1998 standard. Ten profiles were analyzed for PRS and USV treated samples. The measurement was carried out on profiles with a length of 1.25–1.5 mm. According to the EN ISO 4288:1998 standard, for such average roughness values, the minimum length of measurement trace should be 8 mm. However, it was not possible to provide such length because of the small length of the struts between adjacent nodes of lattice.

2.5. Mechanical testing

All scaffolds were mechanically tested in uniaxial compression using universal testing machine INSTRON 3369 by Illinois Tool Works Inc., USA with a maximum load capacity of 50 kN. There are a few standards used today for lattice sample testing, including ISO 13314 (Mechanical testing of metals – Ductility testing – Compression test for porous and cellular
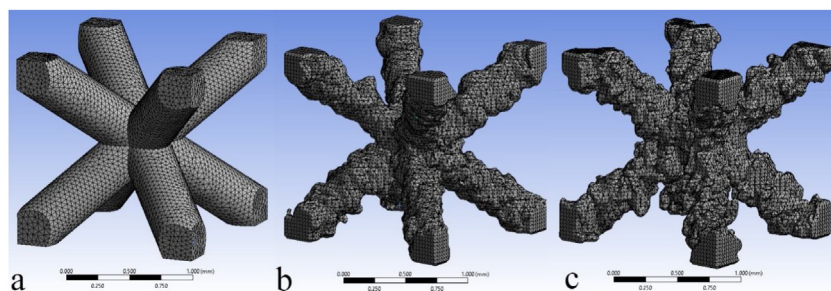
Fig. 3 – BCC cells. (a) BCC cell model, (b) CT-based reconstruction of a cell of PRS treated lattice, (c) CT-based reconstruction of a cell of USV treated lattice.

metals) [30] and Standard Test Methods of Compression Testing of Metallic Materials at Room Temperature [31]. In present study, we have adhered to the ASTM E9 measurement protocol. It was demonstrated that test method according to ASTM E9 standard could be adapted as a standardized one for cellular lattice structures fabricated by AM [32]. In accordance with ASTM E9, compression was performed at a constant rate of 0.5 mm/min. The aspect ratio of the tested sample (i.e., the ratio between the height and outer dimensions) should be between 1.5 and 2 in order to prevent buckling of the scaffolds under compression. Initially, three specimens for both PRS and USV treatment, were compressed along the rotation axis (build direction). However, when it became clear that USV treated specimens behave unpredictably two more specimens were tested to assure the representativeness of the results. The loading was carried out until the samples were compressed to first 30 and then to 50 % strain levels. The elastic modulus E was calculated from the slope of the compressive stress–strain curves in the linear elastic region. The ultimate compressive strength was determined as the maximum stress prior to failure (ASTM E9). The ultimate compressive strain was determined as the strain value corresponding to the ultimate compressive strength.

2.6. Finite element analysis

Following work was carried out to compare the modelled stress distribution in the unit cells of ideal and the manufactured scaffolds. A BCC lattice cell was created with strut thickness corresponding to the average thickness determined from CT data, Fig. 3a. The total amount of nodes and elements in the mesh were equal to 194485 and 134873, respectively. CT-based reconstructions of unit cells with height of 1.5 mm of PRS (Fig. 3b) and USV (Fig. 3c) treated scaffolds were prepared as following. Images of CT-stack were binarized and saved in *.obj format using FiJi ImageJ software considering the size of a voxel. The stack was then opened as a solid body object in SolidWorks 2017 (Dassault Systems, SolidWorks Corporation) and converted to a *.step format for future simulations in ANSYS 19.2 software. The simulation mesh of CT reconstructed lattice cell consisted of 192658 nodes and 113496 elements for the PRS treated scaffold, and 201820 nodes and 118695 elements for the USV treated one. The number of nodes and elements for CT-based reconstructions and theoretically constructed model was approximately the same. Boundary
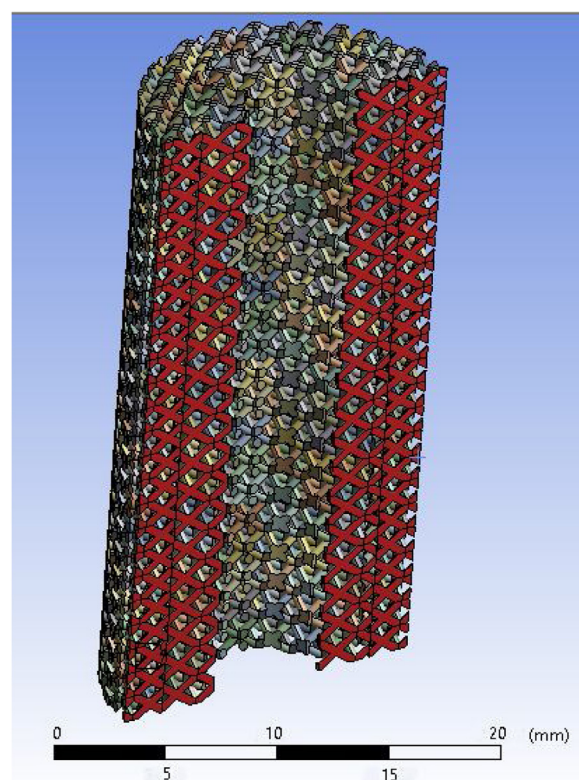

Fig. 4 – SolidWorks model of a 2-zone scaffold.

conditions for the CT-based reconstructions were described as follows: frictionless support was applied to the bottom face; and a normal compressive strain of 3 % was applied from the top face of the cell.

Regular lattices are commonly manufactured with Arcam EBM using the models having zero strut thickness, so that the actual strut thickness is governed by automatically calculated beam control parameters. Usually simulations of large lattice structures'mechanical behavior considered to be very time-consuming and not suitable for the design/optimization of large structures [33]. In our case, actual strut thickness was measured and reconstructed from the CT measurements using FiJi ImageJ software. Source file with zero strut thickness used for printing was not suitable for FEA calculations, since FEA of the linear structure with zero strut thickness would demonstrate only stress distribution between nodes
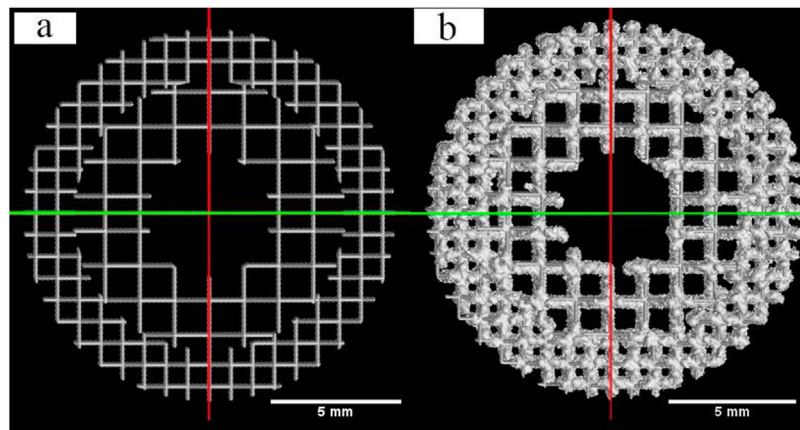
Fig. 5 – Comparative view: (a) model of the functionally graded scaffold, (b) 3D reconstruction of PRS treated with model overlapping.
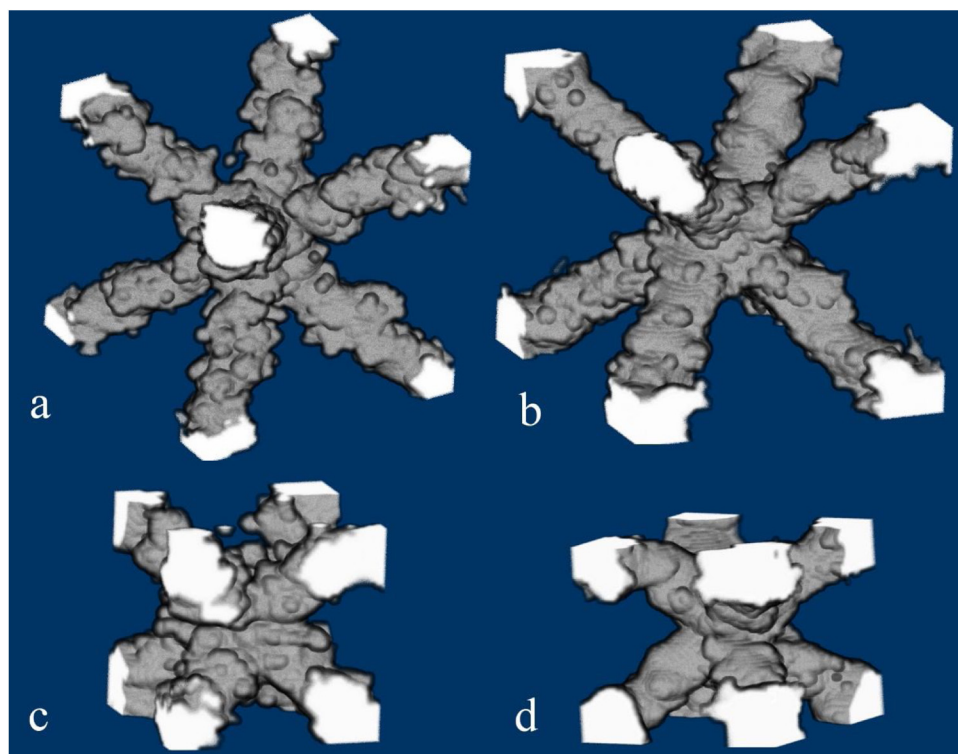
Fig. 6 – Comparative view of 3D rendering of CT reconstructions of the scaffold BCC elements that underwent different cleaning procedures:
(a) Lattice distance of 1.5 mm, USV treated scaffold,
(b) Lattice distance of 1.5 mm, PRS treated scaffold,
(c) Lattice distance of 1.25 mm USV treated scaffold,
(d) Lattice distance of 1.25 mm, PRS treated scaffold,

but not inside individual strut or node. Therefore, the scaffold structure was modeled using SolidWorks 2017 basing on the cell dimensions from the zero-thickness file. As the scaffold has the central plane of symmetry, only half of the structure is needed for the computer modeling, as shown in Fig. 4. Corresponding patterns were constructed from BCC-elements of 1.25 mm and 1.5 mm step length with a strut diameter of 0.4 mm. Cells were repeatedly added in corresponding zones within a single layer covering the footprint of the scaffold cross-section. Next, resulting cross- sectional layer zones with 1.25 and 1.5 mm cells were repeatedly extended over the scaffold length yielding 24 and 20 repetitions, respectively. Then the generated patterns were cut by cylindrical volumetric sections of the diameters corresponding to the ones used in the zero-thickness design file. Because of cutting, thin-walled elements appeared in some places, which were not observed

in real specimens. These elements in stress simulations can generate artificial stress concentrators; therefore, they were manually removed from the final model. Successively, the computation mesh of the full scaffold model was generated resulting in 1166728 nodes and 538080 elements. A symmetry condition was set for the semi-cylindrical model with respect to the central plane of the scaffold making possible to calculate the behavior of the whole scaffold. Boundary conditions were described as frictionless support for the bottom and strain of 3 % for the top of the scaffold, since after mechanical testing it was found that both for PRS and USV treated scaffolds elastic deformation zones extend up to about 3 % strain. Mechanical properties of Ti6Al4V from the built-in ANSYS material library were applied to the CAD-generated and CT-based reconstruction models.

3. Results

3.1. Surface roughness and shape of the scaffolds

As described above, the model of the scaffold used for manufacturing is represented by a straight beam-based structure with zero strut thickness; therefore, the production file indicates only a position for the electron beam in each slice. Strut thickness in a real scaffold is defined by the result of melt pool solidification governed by automatically generated EBM parameter settings. Comparative view of the model for the functionally graded scaffold (from STL-file) and a 3D rendering of CT reconstruction of PRS treated specimen are presented in Fig. 5. Scaffolds with PRS and USV cleaning demonstrated reconstructed strut thickness of $350 \pm 70\,\mu m$ and $430 \pm 60\,\mu m$, respectively. Relatively large standard deviations are due to the significantly non-uniform distribution of strut thickness along a strut. The average roughness (Ra) values for the PRS treated scaffolds were about $74\,\mu m$ with a standard deviation of $8\,\mu m$. USV treated scaffolds have a similar average roughness value of $73\,\mu m$ with a standard deviation of $5\,\mu m$. The mean value of the maximum height on the measured trace (Rt) for a PRS treated scaffold is $231\,\mu m$ with a standard deviation of $32\,\mu m$. For a USV treated scaffold, the mean value is $234\,\mu m$ with a standard deviation of $45\,\mu m$. It is also clear that, in the initial model without strut thickness the inner (coarser mesh) and outer (finer mesh) lattice zones are connected to each other only via occasional strut links (see Fig. 5a). The CT reconstruction data (Fig. 5b) indicate, that due to the real strut thickness many of the gaps present in the model file are closed providing solid metal connections.

The large variation in actual strut thickness is caused by two different mechanisms. Firstly, especially with the thin-strut lattices, the melt pool dimensions become comparable with the strut thickness, leading to the characteristic 'beads on the string' shapes of the lattice struts. Secondly, there are loosely connected and partially fused powder grains, typical for the surfaces of the components manufactured with powder bed fusion AM. In the case of the thin-strut lattices presence of such particles having dimensions comparable to the strut thickness brings additional distortion in the resulting lattice cells. The accuracy of the EBM technology enables to produce lattices with geometry that is very close to the one

Table 1 – Mechanical properties of scaffolds after different powder removal procedures.

	PRS	USV
Mass m, g	5.61 ± 0.19	5.67 ± 0.38
Height h, mm	30.18 ± 0.45	30.26 ± 0.31
Diameter D, mm	15.38 ± 0.32	15.33 ± 0.32
Internal bore diameter d, mm	5.10 ± 0.11	5.05 ± 0.14
Volume V, cm^{3} [a]	4.99 ± 0.22	5.07 ± 0.22
Density ρ, g/cm^3	1.13 ± 0.06	1.13 ± 0.09
Relative density ρ/ρ_0 ($\rho_0 = 4.43\,g/cm^3$)	0.26	0.26
Porosity p, %	74	74
Compressive strength σ_e, MPa	41 ± 2	29 ± 13
Elastic modulus E, GPa [a]	1.19 ± 0.10	0.91 ± 0.40
Yield stress σ_y, MPa	28.5 ± 1.7	24.1 ± 10.5

[a] Elastic modulus and volume were calculated assuming the open core.

demanded by models. The initial state of the specimens cannot be investigated before cleaning procedure. The state of the samples before the USV and PRS treatment were investigated using CT, and struts of approximately demanded diameter with no visible cracks were observed. This proves the integrity of the as-manufactured samples before powder recovery.

Unexpectedly, the experimentally measured strut surface for the PRS treated scaffolds was generally smoother than that for USV treated ones, Fig. 6. The results of the SEM investigation presented in Fig. 7 demonstrate the presence of large numbers of remaining powder particles on the USV treated scaffold strut surfaces, while the PRS treated scaffold surface is almost free of them, Fig. 7b. The increased surface roughness of the struts could cause stress concentrations and promotes crack initiation [33] decreasing fatigue resistance, compressive strength and yield stress of the whole scaffold.

3.2. Mechanical properties and deformation mode

According to results by Rafi et al. [34], typical Young's modulus values measured for Ti6Al4V bulk specimens manufactured with the long sample axis in the build direction ('vertically') and perpendicular to it ('horizontally') are $E_{vert} = 101\,GPa$ and $E_{hor} = 104\,GPa$, respectively. At the same time, the Young's modulus of femoral cortical bone, the strongest load bearing bone in the human body, is about 16-20 GPa [35]. Therefore, the Young's modulus of the ideal scaffold should be sufficiently low for the implementation in orthopedics applications.

In our case, the experimentally measured effective elastic modulus of the PRS treated scaffold is 1.19 GPa, compressive strength- about 41 GPa and the yield stress– about 28 MPa. Mechanical properties of scaffolds that underwent ultrasonic vibration cleaning were substantially worthier. For example, elastic modulus was only 0.91 GPa, and compressive strength was only 29 MPa. All measured mechanical properties of the PRS and USV treated scaffolds are summarized in Table 1. In addition, the USV treated samples exhibit large variations in the mechanical properties, and therefore the mechanical behavior of such samples in service can be quite unpredictable.

Characteristic stress-strain dependencies for the PRS and USV treated scaffolds are presented in Fig. 8a and b, respec-
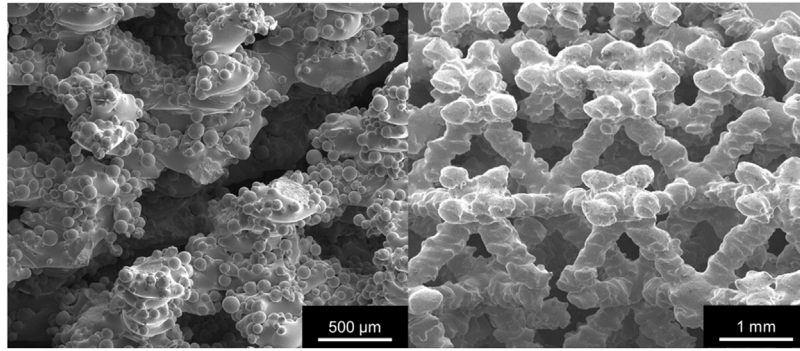
Fig. 7 – SEM images of the scaffold surface morphologies: **(a) USV treatment, (b) PRS treatment.**

tively. Fig. 9 presents images from characteristic vertical 'slices' from the reconstructed CT scans of the deformed PRS and USV treated scaffolds. For both PRS and USV treated scaffolds elastic deformation zones extend up to about 3 % strain. The point of compressive strength for USV treated scaffolds can be observed at approximately 4 % strain (Fig. 8a), while for PRS treated one this value is almost twice higher (Fig. 8b).

It is shown, that elastic behavior in PRS treated scaffold is primarily due to the bending of cell struts, and plastic collapse is mainly initiated at hinges, which is typical for the structures with diagonally oriented struts [36]. During the deformation process the inner call layer struts compact and press out the external zone struts causing a double barrel deformation (Fig. 9a and b). Typical stress-strain curve plateau is slightly extending into a hardening zone, when all diagonal struts are becoming almost horizontal (Figs. 8a and b). Stress value fluctuation within the curve plateau is usually caused by destruction of struts in their thinnest parts (because of the irregular strut thickness).

In general, solid Ti6Al4V alloy is a relatively ductile material [37] and Ti6Al4V scaffolds commonly exhibit ductile behavior up to the failure. The PRS treated scaffolds kept its integrity up to about 50 % strain, but USV treated ones broke into two separate parts after only 5 % strain.

USV treated scaffolds demonstrate completely different fracture mode as compared to the PRS treated ones. USV treated scaffolds do not deform throughout the entire volume, but through one of the diagonal planes (Fig. 8b, c and Fig. 9c, d). Although the stress-strain curves for five USV treated samples showed some discrepancies, diagonal cracks were appearing in every sample (Fig. 8c). Diagonal cracking is typical for the lattice structures consisting of diagonally oriented strut in such structures as rhombic dodecahedron lattice [38] and body centered cubic lattice [39]. The diagonal cracking divides the scaffold into 2 parts, sliding along the fracture plane and causing crumbling. However, the periphery layers of the scaffold lattice remained parallel to the axis of the cylinders until the end of the compression process. As it is typical for such cases, the diagonal plane passes through the specimen closer to one of the edges. The stress-strain dependency of USV treated specimens demonstrates rather random behavior as compared to PRS treated ones, Fig. 9. Since all specimens are taken from the same EBM build and were manufactured using identical parameter settings, and

the difference is only in the powder recovery process applied, it confirms that *local* features changed or generated by the USV treatment are extremely important. With the USV-treated samples the fracture process was accompanied with periodic stress growth after the ultimate compression strength was reached. This can be explained by the collapse of the plane passing through diagonally oriented struts. In addition, as it was found, that the struts of USV treated scaffolds that were not in the immediate proximity of the diagonal plane remained straight during the deformation process, Fig. 9c, d.

The possible impact of the USV treatment can be compared to the effects known for the ultrasonic impact treatment (UIT), a post processing method with immediate contact between a specimen and an actuator designed for improving fatigue stability of the solid parts described by [40]. The energy of vibration creates complex stresses of tension, compression and shear. When the yield stress of the materials is exceeded, plastic deformations occur. Because of plastic deformation and dispersing action of ultrasound the adsorbed liquid films, gases, organic films and surface oxides are removed. Due to this procedure grain refinement in subsurface volume of bulk material can occur. Ultrasonic vibrations have a positive impact on residual stresses relief [40]. For the lattice structures, this effect can differ. The effect of ultrasound treatment with immediate contact between a specimen and an actuator may be dependent on geometry properties of the specimen. For example, initial indications have shown its potential applicability for faster cleaning of the solid (bulk) samples, and its potential applicability for better cleaning of lattice samples was hypothesized.

However, our experiments show that USV treated porous scaffold can become fragile. Lattice scaffolds are much more delicate as compared to the bulk samples, and with USV treatment, cracks are most probably initiated on the strut surfaces causing brittle behavior of the specimens during compression tests. It is also clear, that with USV powder removal more partially fused powder grains are left on the strut surfaces (Figs. 6 and 7), contributing to the stress concentration sites and potentially supporting additional crack generation.

3.3. *Pores*

Non-optimal process parameters, non-ideal thermal properties during the lattice manufacturing may be reasons not only
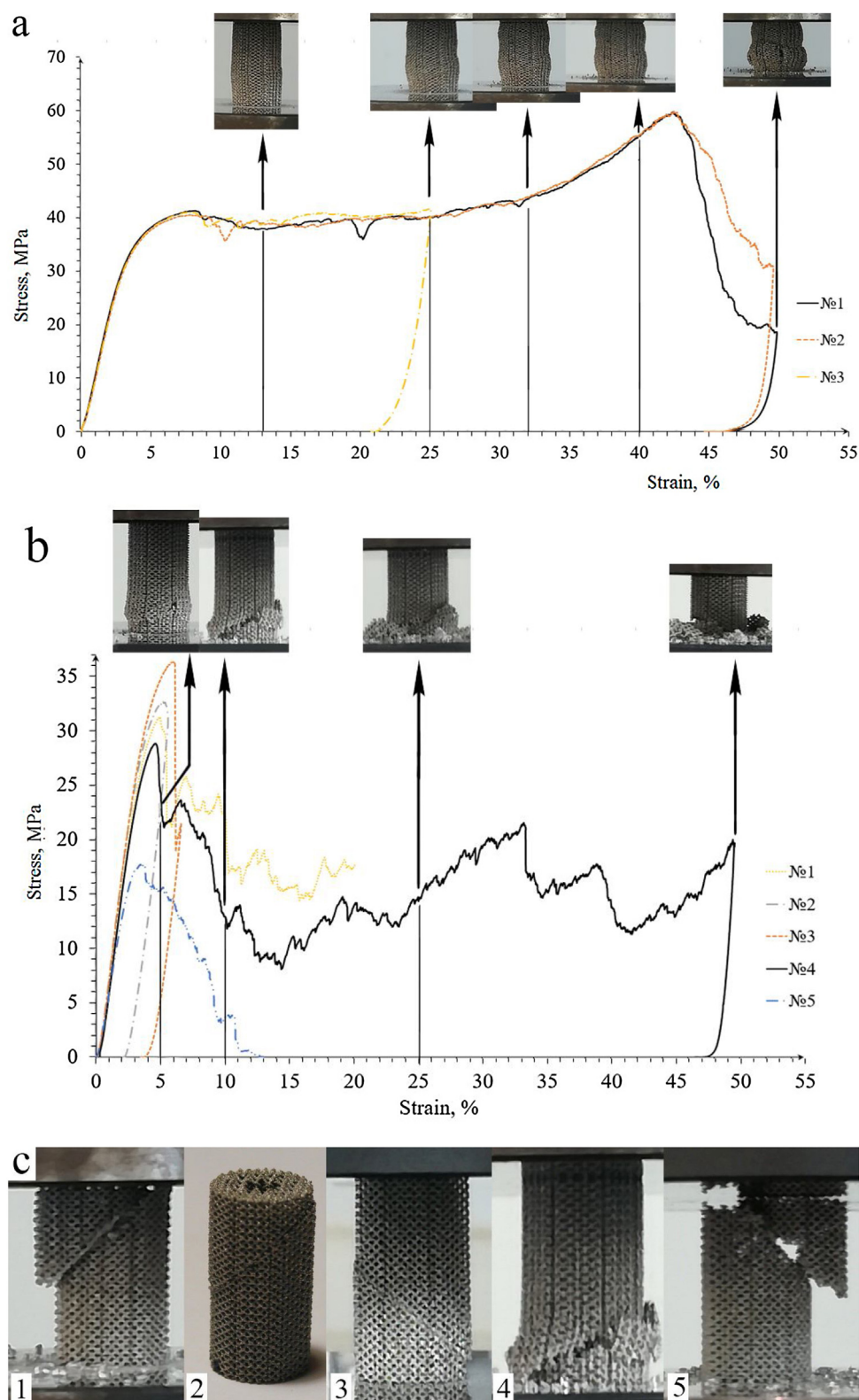
Fig. 8 – (a) Stress-strain dependences for PRS treated scaffolds (b). Stress-strain dependences for USV treated scaffolds (c) photographs of five USV treated samples after failure.

for the presence of partially fused powder particles [41] or cracks [42], but also for the generation of micro voids (pores) in the solid material of the struts [43]. The sphericity of the voids is considered critical for mechanical properties. The sphericity of a particle/void as defined by Wadell [44] is the ratio of the surface area of a sphere with the same volume as the given
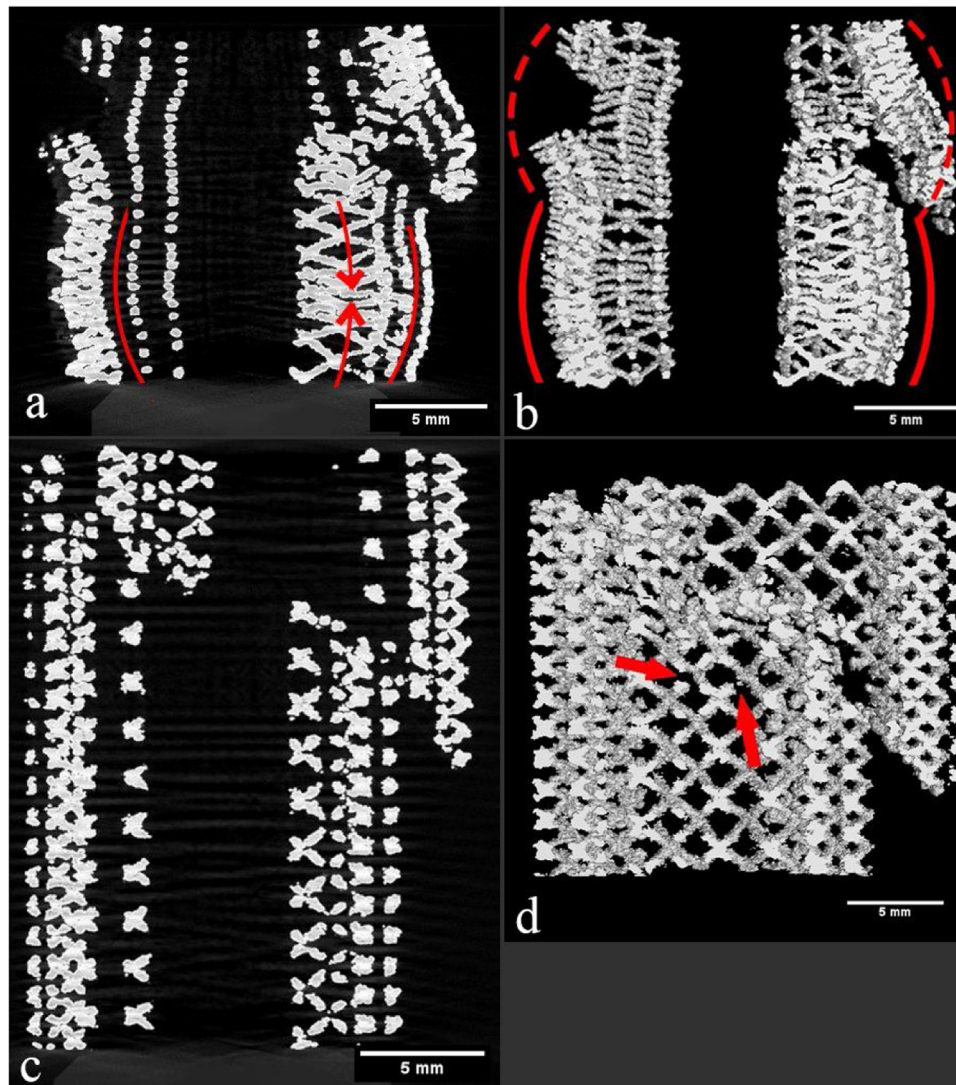
Fig. 9 – The fracture mode representation based on CT-data:
(a) Cross-section of the PRS treated scaffold, (b) A 3D rendering of the PRS treated scaffold,
(c) Cross-section of the USV treated scaffold, (d) A 3D rendering of the USV treated scaffold.

particle/void to the surface area of the particle. Crack-like voids with the sphericity lower than 0.7 may significantly favor crack propagation [45], particularly if they are oriented perpendicular to the tensile load direction. Such defects cause stress concentrations (notch effect), resulting in reduction of static strength of the specimens. Additionally, even small voids in the materials of the thin lattice struts can significantly reduce their mechanical properties and influence the mechanical stability of the whole lattice. One lattice sample from USV and PRS treatment were chosen for the analysis of porosity. The obtained CT data allowed comparing the volume and sphericity of the pores for each type of post-treatment of studied specimens.

The abundance of the pores and crack-like voids differs between PRS and USV treated scaffolds. The relative number of round pores (with sphericity larger than 0.7) in PRS treated specimens is approximately 30 % of all voids, while for the USV treated sample it is about 25 %, Fig. 10a and b. The total amount

of voids detected in USV treated specimen was four times less as compared to the PRS treated one. The largest voids for the USV treated specimens are twice as small as that for PRS treated ones. The sphericity of the voids for both types of samples lays between 0.45 and 0.85. The ratio between the largest pore dimension and the diameter of the strut was about 89 % for PRS treated and 76 % for USV treated scaffolds. However, the differences in pore numbers and sphericity distributions do not allow explaining the observed difference in mechanical behavior in a clear and unambiguous way. Possibly, high intensity vibrations induced in the lattices during USV cleaning can lead to the generation of small cracks (invisible with optical inspection and computed tomography). Different heat treatments such as mill annealing, stress relieving, can influence on density and porosity of an additively manufactured specimens [44]. Hot isostatic pressure (HIP) treatment remains the most powerful method for modifying the material microstruc-
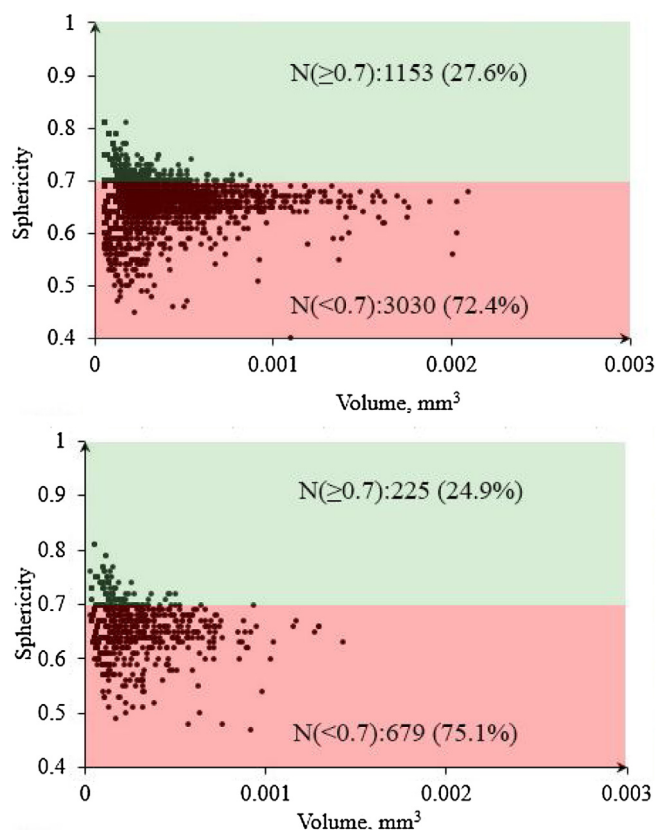
Fig. 10 – Pore sphericity to pore volume relation: (a) For the PRS treated scaffold, (b) for the USV treated scaffold.

ture (e.g. dominant grain sizes, element precipitation between the grains etc.) and decreasing residual porosity [46].

3.4. Fracture surfaces

As described earlier, different post-processing treatment (powder recovery method) cause differences in mechanical characteristics and fracture modes of the specimens. Deformation of the scaffolds treated with PRS was close to ductile, whereas deformation of the specimens treated with USV powder recovery was more fragile. Thus, a difference of the fracture surfaces should also be detectable.

The fracture surface of the struts after the compression tests was examined by SEM. Typical fracture surface images of the PRS treated scaffolds are presented in Fig. 11. At a microscopic level the exhibited features point out to the ductile fracture, with the characteristic dimples and. Similar images of the fracture surfaces of Ti6Al4V can be found elsewhere [47]. Typical fracture surface images of the USV treated scaffolds are presented in Fig. 12. Few opened-up pores on the fracture surface were observed and were indicated with black arrows in Figs. 11 and 12. It is supposed, that the spherical pores were developed during EBM process due to entrapment of gases originally present in gas-atomized metal powders [43]. They play the role of the stress concentrators and the crack initiators. The fracture surface demonstrated mixed mode of ductile and brittle fracture since dimples, randomly

isolated microvoids and quasi-cleavage facets are detected on the fracture surfaces. The stages of the fracture process during compression test of additively manufactured lattice struts was described elsewhere [48]. Typical fracture surface images of specimens with different post-treatment demonstrated microscopic ductile dimples and has no significant difference.

3.5. Finite element analysis

The effective compressive strengths for PRS and USV treated specimens obtained from compression tests using the metamaterial approach are 40 and 29 MPa, correspondingly (Table 1). Such a 'cumulative' approach cannot clearly reveal the influence of the strut surface morphology upon the stress distribution in the individual lattice cell. To evaluate this impact during elastic compression of scaffold, computer simulations using the models of BCC element (idealized model) and CT-based reconstruction of BCC elements from PRS and USV treated scaffold were performed. A compressive strain of 3 % was chosen for this evaluation.

Fig. 15 illustrates the results of simulating compression experiments on the three models and depicts corresponding von Mises stress contours with 3 % strain. The formation of tension and compression zones was observed at the opposite surfaces of each strut of the idealized BCC, lattice cell (Fig. 13, diagonal cross-sections, Model). High stress areas are concentrating at the node centers (Fig. 13, diagonal and longitudinal cross-sections, Model). Simulated compression for the CT-based reconstructions reveals some additional details. Sharp edges formed by the incoming struts in the node areas of the ideal model are the main stress concentrators, with the calculated stress values reaching 1 GPa. Due to the process imperfections, these areas are rounded in the manufactured scaffolds. However, due to the surface roughness in the area where two struts are joining multiple stress concentrators are present, and calculated stress values in these areas reaches 1.1 GPa for PRS treated scaffold and 1.2 GPa for USV treated one, Fig. 13. Generally, simulations using idealized and reconstructed cell models indicate that highest stress values are occurring around the nodes, especially at the places where the struts are joining at small angles. It is also clear that significant differences between stress distributions in the reconstructed and the idealized model are caused by the actual surface morphology of each particular strut. Some unstressed, partially fused, metal particles can be observed on the surface of the struts. The more they protrude over the surface the less they influence overall stress distribution. Larger clusters of partially molten particles may significantly increase the local cross-section of the strut, thus influencing the stress distribution picture. It is clear, that in the situation of the lattices with thin struts the surface morphology will have quite significant impact on the overall mechanical properties of the sample. This would be especially pronounced in the cases when the average roughness values become comparable in size to the strut thickness, and when defects such as partially fused or loosely connected powder grains are present on the surface.

The full-scale model of the two-zone scaffold was also used to evaluate stress distribution during elastic compression. As mentioned earlier, 1.25 and 1.5 mm cells were repeatedly posi-
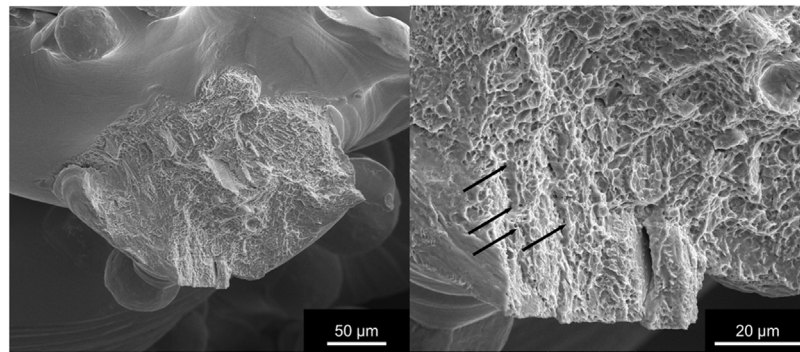
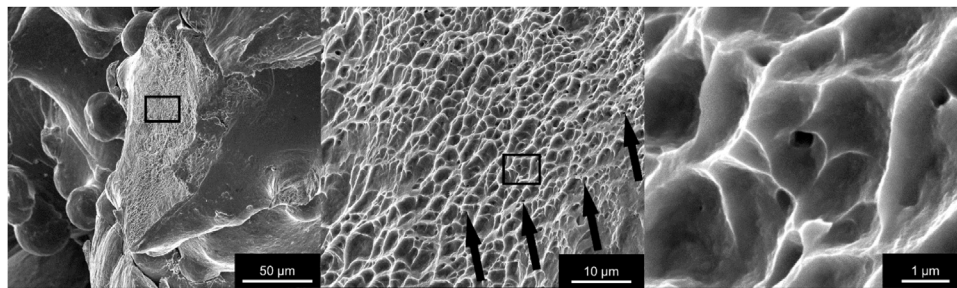**Fig. 11 – Typical USV treated scaffold fracture surface images.**

Fig. 12 – Typical PRS treated scaffold fracture surface images.
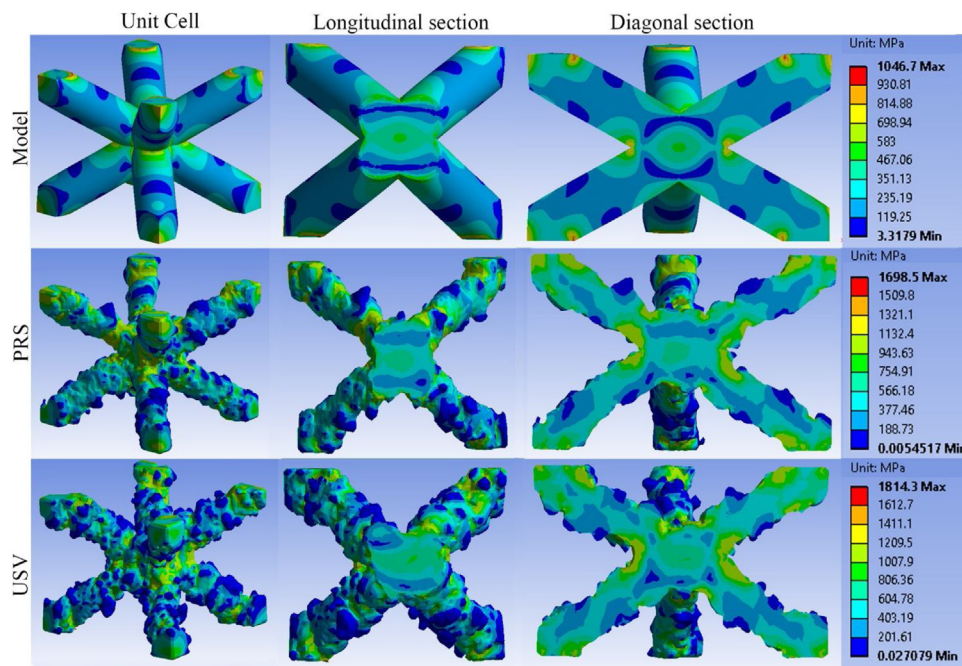

Fig. 13 – Von Mises stress contours in BCC cell idealized model (Model), CT reconstruction of a cell for PRS treated lattice (PRS), and USV treated lattice (USV).

tioned over the height of the sample in 24 and 20 horizontal layers, respectively. Because of the dimension mismatch, lattice struts of some cells in the inner structure layer are not connected or just partially connected to the elements of the neighboring lattice elements of the outer layer. It is clearly observed in both idealized model and the CT reconstruction of manufactured scaffold. Fig. 14 presents the of stress distribution simulation for the axial loading of the reconstructed scaffold model in the longitudinal (Fig. 14a) and transversal (Fig. 14c) cross-sections. Fig. 14b presents a CT image of the scaffold with clearly visible mismatch defects. Such defects are also visible in the cross-section of the reconstructed model used for simulations (Fig. 14c). With the common way of scaffold structure geometry generation used, the presence of such
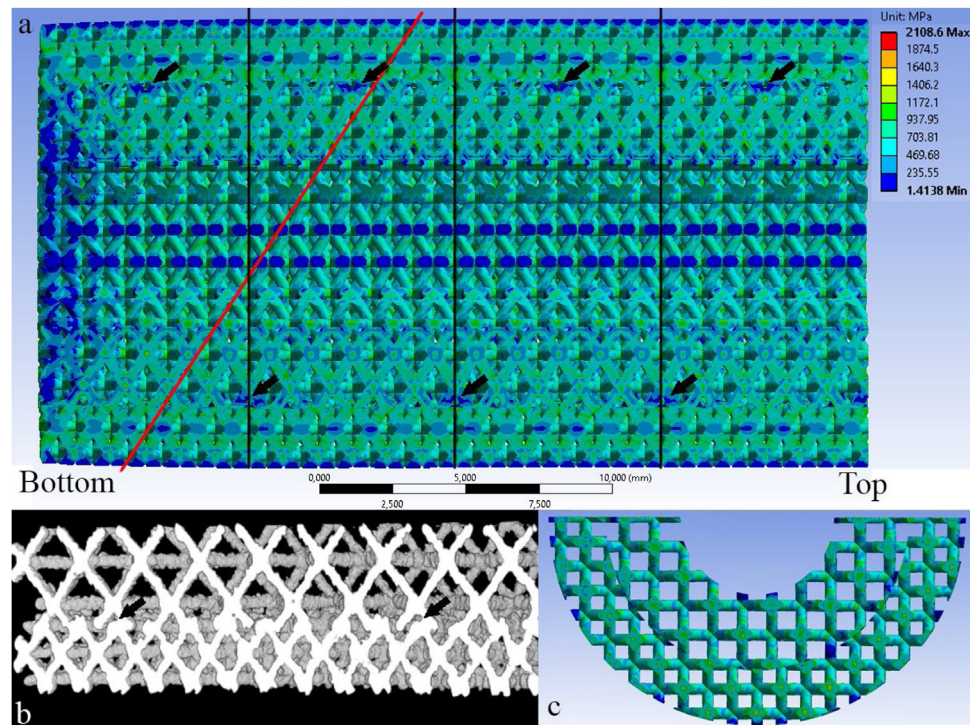
Fig. 14 – (a) Stress distribution in scaffold model, longitudinal section, side view, (b) 3D rendering of CT reconstruction of the scaffold fragment, (c) Stress distribution in scaffold model, transverse section, top view. Black arrows mark the areas with largest mismatch, producing virtually stress- free zones in the lattice intersection plane. Red line indicates observed failure plane of one of the USV treated scaffolds.

mismatch defects is unavoidable. It is also noticeable that, due to the periodicity of both inner and outer lattice structure zones, the areas of largest mismatch (marked by black arrows in Fig. 14a) will periodically be followed by almost perfect matching, producing virtually stress-free zones in the lattice intersection plane. This periodic repetition of areas with significant number of disconnected lattice cell elements in the plane separating two lattice zones could be one of the reasons for a double barrel formation with vertically offset bulging on the sides, observed during mechanical testing (Fig. 9a, b). Based on the 7.5 mm offset of the almost stress free zones on the opposite sides of the cylinder separating two lattice zones (Fig. 14a), one can predict similar separation of the zones with large numbers of mismatch defects and disconnected struts. Taking into account that the diameter of this cylinder is 11 mm the failure plane coming through the inclined 'maximum mismatch belt' should be inclined about 32 degrees from horizontal, which matches well with the experimental observations (Figs. 9 and 10).

Moreover, one can argue that the von Mises stress grows faster as a function of stress in the lattice sample periphery (zone with denser lattice). According to the simulation results, the largest stress appears in the center of nodes (about 1.5 GPa), which is twice as high as the average stress in the struts (0.7 GPa). However, the node failure is not observed in the simulations (see Fig. 9).

The mismatch of cell dimensions in adjacent lattice zones leaving disconnected cell elements is a serious challenge in designing gradient lattice structures. The transition between areas with different porosity should be as gradual as possible leaving smallest numbers of free hanging struts that can cause unpredictable behavior and bad mechanical properties of the whole structure.

4.   Discussion

PRS treated scaffolds demonstrate significantly differing mechanical properties and completely different fracture mode as compared to the USV treated ones. The PRS treated scaffold retains its integrity until 50 % strain, while the USV treated one splits into two separate parts after only 5 % strain. The USV treated scaffolds do not deform throughout the entire volume, but through one of the diagonal planes, and undergo a fragile fracture.

The measured Young's moduli are equal to 1.19 and 0.96 GPa for PRS and USV treated two-zone scaffolds, respectively. Ultrasonic post treatment significantly reduces the compressive strength from 41 to 29 MPa as compared to standard PRS treatment. The ultimate compressive strength of USV treated specimens shows large spread of measured values, making predictions of the mechanical behavior of the structures with such powder removal quite problematic: because of the influence of surface features, the behavior of such structures is highly influenced by statistics (analogous to monolithic brittle materials). Such statistical treatment is outside the scope of the present work.

The stress distributions in the idealized BCC lattice cell model (with struts shaped as ideal cylinders) and in the cell

model reconstructed from the CT scans are also different. This is mainly due to the rough surface profile formed by partially fused metal powder particles and rounding of the angles between joining struts due to the manufacturing process imperfections. Small size surface imperfections around the strut joints provide multiple stress concentrators and leading to the increasing stress values. Powder grains that are partially fused and loosely connected to the surface of struts are showing very low simulated stress levels. These grains protrude over the surface of the strut and only marginally influence the overall stress distribution. The situation becomes different when such grains form large clusters on the strut surfaces, significantly changing local strut cross-section.

The periodicity of the stress distribution of a two-zone scaffold model is connected with the periodic joining mismatch between the struts of the cells from inner and outer zones. The failure surface inclination angle of the broken USV treated scaffold coincides with the inclination of the belt-like area of joining mismatch coming through the cylindrical surface separating the two lattice zones. This belt-like area has the largest number of mismatch defects and free hanging struts. Presumably, this joining mismatch is also one of the reasons for a double-barrel deformation behavior of the USV treated two-zone scaffold showing similar inclination of the bulges on different sides of the sample.

5. Concluding remarks

Mechanical properties and mechanical behavior of two-zone scaffolds subjected to different powder recovery treatment, using ARCAM powder recovery system (PRS) and ultrasound vibration (USV) were investigated. Two main aspects can be identified to summarize the mechanical behavior of two-zone scaffolds. Microscopic investigation shows that the surface of scaffolds that underwent USV cleaning has a larger number of partially fused powder particles on the surface of material as compared to the scaffold cleaned with PRS. This increases surface roughness of the struts, causes stress concentrations and provides additional crack initiation sites, thereby decreasing compressive strength and yield stress of the whole scaffold. Additionally, high intensity vibrations induced in the lattice during USV cleaning with direct contact of the vibration head and lattice samples can lead to the generation of small cracks (invisible with optical inspection and with computed tomography). These two features are reflected in the characteristic stress-strain behavior of the loaded scaffolds. In addition, the fracture surface analysis of PRS treated scaffolds displays typical ductile behavior. Fracture surfaces of the USV treated sample reveal indications of the mixture of brittle and ductile fracture features.

From the macroscopic point of view, a significant number of joining mismatch defects leading to disconnected lattice elements exist along the surface separating the two lattice zones with different lattice cell dimensions. Areas with a large number of such defects are periodic, with the period determined by the difference in the dimensions of the elementary cells. From the metamaterial point of view, results of the experimental studies clearly show that USV method of powder recovery can result in degradation of critical effective mechanical proper-

ties of the lattice samples. We conclude that though scaffold ultrasonic cleaning with direct actuator contact to the components is significantly faster as compared to the PRS based one, defects that can be introduced by the direct contact can be very detrimental. Small cracks potentially introduced by USV post processing can be left undetected even with such advanced method as CT, threatening a component failure during service life. Most probably, SLM manufactured structures will also degrade under after USV treatment. Thus, obtained results reveal that PRS post treatment procedure is still a better choice for removing semi-sintered powder from lattice containing and porous scaffolds manufactured by EBM, and USV treatment is not recommended. Alternative methods of semi-sintered powder removal should be considered in the situations when the traditional PRS powder removal is not effective. Further efforts should be undertaken to find better and more effective semi-sintered powder removal method suitable for both solid and porous EBM-manufactured components. It is also clear that additional research is definitely needed to identify the approach towards the effective computer-supported generation of the scaffolds with gradually changing porosity free of 'joining mismatch' defects.

Conflict of interest

The authors declare no conflict of interests.

Acknowledgements

REFERENCES

[1] van Grunsven W, Hernandez-Nava E, Reilly G, Goodall R. Fabrication and mechanical characterisation of titanium lattices with graded porosity. Metals (Basel) 2014;4:401–9, http://dx.doi.org/10.3390/met4030401.

[2] Heinl P, Mu L, Singer RF, Mu FA, Ko C. Cellular Ti – 6Al – 4V structures with interconnected macro porosity for bone implants fabricated by selective electron beam melting. Acta Biomater 2008;4:1536–44, http://dx.doi.org/10.1016/j.actbio.2008.03.013.

[3] Ma T, Lei W, Wang L, Feng Y, Wang J, Shi L, et al. Evaluation of an artificial vertebral body fabricated by a tantalum-coated

porous titanium scaffold for lumbar vertebral defect repair in rabbits. Sci Rep 2018;8:1–11, http://dx.doi.org/10.1038/s41598-018-27182-x.

[4] Harrysson OLA, Cansizoglu O, Marcellin-Little DJ, Cormier DR, West HA. Direct metal fabrication of titanium implants with tailored materials and mechanical properties using electron beam melting technology. Mater Sci Eng C 2008;28:366–73, http://dx.doi.org/10.1016/j.msec.2007.04.022.

[5] Ryan G, Pandit A, Apatsidis DP. Fabrication methods of porous metals for use in orthopaedic applications. Biomaterials 2006;27:2651–70, http://dx.doi.org/10.1016/j.biomaterials.2005.12.002.

[6] Amin Yavari S, Ahmadi SM, Wauthle R, Pouran B, Schrooten J, Weinans H, et al. Relationship between unit cell type and porosity and the fatigue behavior of selective laser melted meta-biomaterials. J Mech Behav Biomed Mater 2015;43:91–100, http://dx.doi.org/10.1016/j.jmbbm.2014.12.015.

[7] Wu YC, Kuo CN, Shie MY, Su YL, Wei LJ, Chen SY, et al. Structural design and mechanical response of gradient porous Ti-6Al-4V fabricated by electron beam additive manufacturing. Mater Des 2018;158:256–65, http://dx.doi.org/10.1016/j.matdes.2018.08.027.

[8] Maskery I, Aboulkhair NT, Aremu AO, Tuck CJ, Ashcroft IA, Wildman RD, et al. A mechanical property evaluation of graded density Al-Si10-Mg lattice structures manufactured by selective laser melting. Mater Sci Eng A 2016;670:264–74, http://dx.doi.org/10.1016/j.msea.2016.06.013.

[9] Xiao L, Song W. Additively-manufactured functionally graded Ti-6Al-4V lattice structures with high strength under static and dynamic loading: experiments. Int J Impact Eng 2018;111:255–72, http://dx.doi.org/10.1016/j.ijimpeng.2017.09.018.

[10] Han C, Li Y, Wang Q, Wen S, Wei Q, Yan C, et al. Continuous functionally graded porous titanium scaffolds manufactured by selective laser melting for bone implants. J Mech Behav Biomed Mater 2018;80:119–27, http://dx.doi.org/10.1016/j.jmbbm.2018.01.013.

[11] Persenot T, Martin G, Dendievel R, Bu J, Maire E. Enhancing the tensile properties of EBM as-built thin parts: effect of HIP and chemical etching materials characterization. Mater Characterisation 2018, http://dx.doi.org/10.1016/j.matchar.2018.01.035.

[12] Xiao L, Song W, Hu M, Li P. Compressive properties and micro-structural characteristics of Ti–6Al–4V fabricated by electron beam melting and selective laser melting. Mater Sci Eng A 2019;764:138204, http://dx.doi.org/10.1016/j.msea.2019.138204.

[13] Wysocki B, Idaszek J, Szlazak K, Strzelczyk K, Brynk T, Kurzydłowski KJ, et al. Post processing and biological evaluation of the titanium scaffolds for bone tissue engineering. Materials (Basel) 2016;9, http://dx.doi.org/10.3390/ma9030197.

[14] Drescher P, Reimann T, Seitz H. Investigation of powder removal of net-structured titanium parts made from electron beam melting. Int J Rapid Manuf 2014;4:81–9, http://dx.doi.org/10.1504/IJRAPIDM.2014.066007.

[15] Yan C, Hao L, Hussein A, Wei Q, Shi Y. Microstructural and surface modifications and hydroxyapatite coating of Ti-6Al-4V triply periodic minimal surface lattices fabricated by selective laser melting. Mater Sci Eng C 2017;75:1515–24, http://dx.doi.org/10.1016/j.msec.2017.03.066.

[16] Hasib H, Harrysson OLALA, Ii HAW. Powder removal from Ti-6Al-4V cellular structures fabricated via electron beam melting. XXXX 2015;67:639–46, http://dx.doi.org/10.1007/s11837-015-1307-x.

[17] Van Hooreweder B, Apers Y, Lietaert K, Kruth JP. Improving the fatigue performance of porous metallic biomaterials

produced by selective laser melting. Acta Biomater 2017;47:193–202, http://dx.doi.org/10.1016/j.actbio.2016.10.005.

[18] Pyka BG, Burakowski A, Kerckhofs G, Moesen M, Van Bael S, Schrooten J, et al. Surface modification of Ti6Al4V open porous structures produced by additive manufacturing. Adv Eng Mater 2012;14:363–70, http://dx.doi.org/10.1002/adem.201100344.

[19] Yu W, Sing SL, Chua CK, Tian X. Influence of re-melting on surface roughness and porosity of AlSi10Mg parts fabricated by selective laser melting. J Alloys Compd 2019;792:574–81, http://dx.doi.org/10.1016/j.jallcom.2019.04.017.

[20] Marimuthu S, Triantaphyllou A, Antar M, Wimpenny D, Morton H, Beard M. Laser polishing of selective laser melted components. Int J Mach Tools Manuf 2015;95:97–104, http://dx.doi.org/10.1016/j.ijmachtools.2015.05.002.

[21] Vaithilingam J, Goodridge RD, Hague RJM, Christie SDR, Edmondson S. The effect of laser remelting on the surface chemistry of Ti6al4V components fabricated by selective laser melting. J Mater Process Technol 2016;232:1–8, http://dx.doi.org/10.1016/j.jmatprotec.2016.01.022.

[22] Ahmed N, Abdo BM, Darwish S, Moiduddin K, Pervaiz S, Alahmari AM, et al. Electron beam melting of titanium alloy and surface finish improvement through rotary ultrasonic machining. Int J Adv Manuf Technol 2017;92:3349–61, http://dx.doi.org/10.1007/s00170-017-0365-3.

[23] Tan KL, Yeo SH. Surface modification of additive manufactured components by ultrasonic cavitation abrasive finishing. Wear 2017:378–9, http://dx.doi.org/10.1016/j.wear.2017.02.030, 90–5.

[24] Lyczkowska E, Szymczyk P, Dybała B, Chlebus E. Chemical polishing of scaffolds made of Ti-6Al-7Nb alloy by additive manufacturing. Arch Civ Mech Eng 2014;14:586–94, http://dx.doi.org/10.1016/j.acme.2014.03.001.

[25] Biamino S, Penna A, Ackelid U, Sabbadini S, Tassa O, Fino P, et al. Electron beam melting of Ti e 48Al e 2Cr e 2Nb alloy: microstructure and mechanical properties investigation. Intermetallics 2011;19:776–81, http://dx.doi.org/10.1016/j.intermet.2010.11.017.

[26] Surmeneva MA, Surmenev RA, Chudinova EA, Koptioug A, Tkachev MS, Gorodzha SN, et al. Fabrication of multiple-layered gradient cellular metal scaffold via electron beam melting for segmental bone reconstruction. Mater Des 2017;133:195–204, http://dx.doi.org/10.1016/j.matdes.2017.07.059.

[27] Maskery I, Aremu AO, Simonelli M, Tuck C, Wildman RD, Ashcroft IA, et al. Mechanical properties of Ti-6Al-4V selectively laser melted parts with body-centred-Cubic lattices of varying cell size. Exp Mech 2015;55:1261–72, http://dx.doi.org/10.1007/s11340-015-0021-5.

[28] Smith CJ, Derguti F, Tammas-williams S, Leonard F, Hern E, Withers PJ, et al. The effect of defects on the mechanical response of Ti-6Al-4V cubic lattice structures fabricated by electron beam melting. Acta Mater 2016;108:279–92, http://dx.doi.org/10.1016/j.actamat.2016.02.029.

[29] Kruth JP, Bartscher M, Carmignato S, Schmitt R, De Chiffre L, Weckenmann A. Computed tomography for dimensional metrology. CIRP Ann Manuf Technol 2011;60:821–42, http://dx.doi.org/10.1016/j.cirp.2011.05.006.

[30] International organization for Standartization. Mechanical testing of metals — ductility testing — compression test for porous and cellular metals; 2011, doi: ISO 13314:2011.

[31] ASTM-E9-89a. Standard test methods of compression testing of metallic materials at room temperature, vol. 03.01. West Conshohocken, PA: ASTM International; 2000, http://dx.doi.org/10.1520/E0009-89AR00.

[32] Sing SL, Yeong WY, Wiria FE, Tay BY. Characterization of titanium lattice structures fabricated by selective laser

melting using an adapted compressive test method. Exp Mech 2016;56:735–48, http://dx.doi.org/10.1007/s11340-015-0117-y.

[33] Wauthle R, Amin Yavari S, Janssen M, Riemslag AC, Zadpoor AA, Ahmadi SM, et al. Effects of bio-functionalizing surface treatments on the mechanical behavior of open porous titanium biomaterials. J Mech Behav Biomed Mater 2014;36:109–19, http://dx.doi.org/10.1016/j.jmbbm.2014.04.010.

[34] Rafi HK, Karthik NV, Starr TL, Stucker BE. Mechanical property evaluation of Ti-6Al-4V parts made using electron beam melting. Solid Freeform Fabr Symp Proc 2012:526–35.

[35] Katsamanis F, Raftopoulos DD. Determination of mechanical properties of human femoral cortical bone by the Hopkinson bar stress technique. J Biomech 1990;23:1173–84, http://dx.doi.org/10.1016/0021-9290(90)90010-Z.

[36] Gibson LJ, Ashby MF. The mechanics of three-dimensional cellular materials. Proc R Soc A Math Phys Eng Sci 2006;382:43–59, http://dx.doi.org/10.1098/rspa.1982.0088.

[37] Xu W, Brandt M, Sun S, Elambasseril J, Liu Q, Latham K, et al. Additive manufacturing of strong and ductile Ti-6Al-4V by selective laser melting via in situ martensite decomposition. Acta Mater 2015;85:74–84, http://dx.doi.org/10.1016/j.actamat.2014.11.028.

[38] Lijun T, X WDX, Fan DXX, Jianzhong DX. Mechanical properties of open-cell rhombic dodecahedron titanium alloy lattice structure manufactured using electron beam melting under dynamic loading. Int J Impact Eng 2017;100:75–89, http://dx.doi.org/10.1016/j.ijimpeng.2016.10.006.

[39] Frith J, Onal E, Wu X, Molotnikov A, Jurg M. Mechanical properties and in vitro behavior of additively manufactured and functionally graded Ti6Al4V porous scaffolds. Metals (Basel) 2018;8:200, http://dx.doi.org/10.3390/met8040200.

[40] Panin VE, Kablov EN, Pleshanov VS, Klimenov VA, Ivanov YF, Pochivalov YI, et al. Effect of ultrasonic shock treatment on the structure and fatigue strength of welded joints of high-strength steel VKS-12. Phys Mesomech 2006;2:85–96.

[41] Zhao S, Li SJ, Hou WT, Hao YL, Yang R, Misra RDK. The influence of cell morphology on the compressive fatigue behavior of Ti-6Al-4V meshes fabricated by electron beam melting. J Mech Behav Biomed Mater 2016;59:251–64, http://dx.doi.org/10.1016/j.jmbbm.2016.01.034.

[42] Osakada K, Shiomi M. Flexible manufacturing of metallic products by selective laser melting of powder. Int J Mach Tools Manuf 2006;46:1188–93, http://dx.doi.org/10.1016/j.ijmachtools.2006.01.024.

[43] Gong H, Rafi K, Gu H, Janaki Ram GD, Starr T, Stucker B. Influence of defects on mechanical properties of Ti-6Al-4V components produced by selective laser melting and electron beam melting. Mater Des 2015;86:545–54, http://dx.doi.org/10.1016/j.matdes.2015.07.147.

[44] Wadell H. Volume, shape, and roundness of quartz particles. J Geol 1935;43:250–80, http://dx.doi.org/10.1086/624298.

[45] Kasperovich G, Haubrich J, Gussone J, Requena G. Correlation between porosity and processing parameters in TiAl6V4 produced by selective laser melting. Mater Des 2016;112:160–1, http://dx.doi.org/10.1016/j.matdes.2016.09.040.

[46] Ahmadi SM, Kumar R, Borisov EV, Petrov R, Leeflang S, Li Y, et al. From microstructural design to surface engineering: a tailored approach for improving fatigue life of additively manufactured meta-biomaterials. Acta Biomater 2019;83:153–66, http://dx.doi.org/10.1016/j.actbio.2018.10.043.

[47] Bruno J, Rochman A, Cassar G. Effect of build orientation of Electron beam melting on microstructure and mechanical properties of Ti-6Al-4V. J Mater Eng Perform 2017;26:692–703, http://dx.doi.org/10.1007/s11665-017-2502-4.

[48] Adkins NJE, Yue S, Qiu C, Withers PJ, Lee PD, Attallah MM, et al. Influence of processing conditions on strut structure and compressive properties of cellular lattice structures fabricated by selective laser melting. Mater Sci Eng A 2015;628:188–97, http://dx.doi.org/10.1016/j.msea.2015.01.031.